High Sensitivity Long-Wave Infrared Detector Design Based on Integrated Plasmonic Absorber and VO$_2$ Nanobeam

Mohammad Wahiduzzaman Khan, Jonathan Matthew Sullivan, Jaeho Lee, and Ozdal Boyraz

Abstract—We report a novel design for bolometric infrared detector operating at the long-wave infrared (LWIR) range for high-resolution human body temperature sensing and monitoring. We propose to incorporate efficient plasmonic absorber and high-responsivity VO$_2$ nanobeam biased at transition temperature in our design to facilitate improvement in both aspects – thermal resolution and spatial resolution. The integration of plasmonic absorber allows efficient and selective radiation absorption. The use of a transducing nanobeam placed in close proximity to the plasmonic local heaters allows the radiation energy to be electronically readable. The use of nanobeam instead of a film in the detector allows over two-orders of magnitude improvement in responsivity owing to the large length to cross-sectional area ratio. Additionally, the use of nanobeam reduces the thermal mass and improves the bandwidth. Our calculation suggests a responsivity of as high as 700 kV/W at 100 Hz for a detector of only 12 μm × 12 μm pixel size. Also, the theoretical noise equivalent temperature difference is calculated to be as low as 3.67 mK which is almost an order of improvement than the state-of-the-art bolometric LWIR detectors with larger pixel dimensions.

Index Terms—Bolometer, infrared detector, LWIR, plasmonic absorber, vanadium dioxide.

I. INTRODUCTION

THE two main types of infrared (IR) detectors are thermal detector and photon detector. The thermal detectors function based on the principles of temperature dependent phenomena - change in resistance, voltage generation in junction, change in polarization, thermal expansion of gas, etc. On the other hand, photon detectors functions by converting IR radiation into photo generated free carriers [1]. At present, high-performance infrared imaging technology is mainly based on epitaxially grown structures of the small-bandgap bulk alloy mercury-cadmium-telluride (MCT) [2], [3]. Quantum-well infrared photodetectors based on InSb, GaAs, InGaAs and others are also available. However, these technologies require

very low operating temperature ($<$ 240 K) increasing the bulkiness and cost of the system [1], [2]. The need for increased performance of the infrared detectors has driven extensive research towards the improvement in current IR detection technology as well as spurred novel techniques and sensors [4]–[6]. The advancement of integrated optics [7]–[10] and photonic integrated circuits has brought forward both IR detection and readout capability in the same chip [11]–[13]. However, there is still requirement for higher sensitivity and higher pixel density detectors for critical applications and high-resolution thermal imaging and sensing for medical and military purposes. Phase-changing materials (PCM) hold significant potential in optical and thermal sensing and switching due to their sharp temperature dependent characteristics. Vanadium dioxide (VO$_2$) is the most utilitarian PCM because of its close-to-room-temperature transition point. Most commonly reported value for this semiconductor-to-metal transition temperature of VO$_2$ films is 68°C [14]. However, the film and deposition technique can be engineered to further lower the transition even closer to the room-temperature [15], [16] with a narrower hysteresis. At the transition point, resistivity of VO$_2$ material undergoes over three [14] to four [17] orders of change in magnitude. VO$_2$-based bolometers utilize the material's large temperature coefficient of resistivity (TCR) [16], [18] to detect infrared radiation. The VO$_2$ film can be nanoengineered [16], [19], [20] to improve bolometer sensitivity. In addition, there has been development on MEMS-based bolometers [21] and integration of patterned coating [22] for improved performance. However, the active radiation absorption area still needs to be large enough that allows sufficient temperature buildup from incident radiation absorbed by VO$_2$, thus requiring large pixel dimension and degrading the spatial resolution of bolometric sensing. The fabrication process dependence and close co-existence of different oxides [23]–[27] of the deposited vanadium films pose challenges in obtaining high-TCR film thus degrading detector performance. Moreover, the absorption by the VO$_2$ material is not optimized for a specific frequency band in most of the applications. Nanostructured or nanobeam VO$_2$ has been used to compensate the degradation of TCR and achieve higher sensitivity [16], [28]. On the other hand, to achieve increased absorption for a specific band of incident radiation by reduced-size pixel, plasmonic micro- and nanostructures [29]–[32] can be designed and tuned. The VO$_2$ nanobeam

and plasmonic nanostructures thus have the potential to be incorporated together for sensitive bolometric detection. The prevalent design dilemma between the obtained thermal resolution and spatial resolution, bolometric bandwidth and performance, sensitivity and noise need to be analyzed in order to achieve an optimized detector.

In this work, we propose a novel infrared detector architecture that integrates efficient, selective, and scalable plasmonic absorber with high-sensitivity VO_2 nanobeam transducer. To the best of our knowledge, this is the first report on room-temperature IR detector comprising integrated plasmonic absorber and VO_2 nanobeam. The goal of the proposed design is to improve both – thermal resolution as well as spatial resolution and to address the challenge of low thermal contrast at long wavelength infrared (LWIR). To achieve the maximum sensitivity, we propose to operate the detector at the transition temperature to exploit the high TCR of VO_2. We present the numerical analysis to show the mid-infrared radiation absorption characteristic of the detector, particularly the plasmonic absorber and estimate the resultant local heating. The use of VO_2 nanobeam instead of a thin-film allows amplified temperature-dependent resistance thus a larger slope of impedance variation in response to local heating by radiation absorption. The performance, bandwidth, and noise analysis of the integrated detector designed for LWIR detection for human body as the radiation-emitting object (310 K or 10 μm wavelength) are also presented. We estimate the responsivity of the proposed detector to be over 700 kV/W at 100 Hz with ultra-low noise equivalent temperature difference (NETD) in a small footprint pixel size of 12 μm by 12 μm.

II. DESIGN

Proposed design has three main components: radiation absorber, VO_2 nanobeam, support structure with thermal isolation. Radiation absorber is the key component that determines the absorption efficiency, and it consists of single to multiple unit cells of plasmonic absorber. VO_2 nanobeam integrated with the plasmonic absorber functions as the transducing or sensing material. The support structure allows the suspension of the detector pixel and allow thermal isolation. The schematic of a single pixel with 9 absorber unit cells are depicted in Fig. 1(a). The unit cell schematic and cross-section including the dimensions are presented in Fig. 1(b). The number of unit cells present in a single pixel of the proposed infrared detector is scalable and depends on the absorbed power required for sufficient thermal buildup which, in turn, depends on the thermal isolation of the pixels. For our design, we have chosen the bolometer pixel with 3×3 unit cells as a balance of improvement between thermal resolution and spatial resolution. Larger number of unit cells will capture more radiation power that will result in increased thermal buildup ultimately resulting in a higher responsivity. However, larger pixel dimension will reduce the spatial resolution and degrade the thermal bandwidth of the detector. In this report, we only focus on the elements in a single pixel and select a conventional design for the pixel – suspension, support membrane, arms, etc. The optimization of the pixel structure,

arm, suspension can be furthered to enhance thermal isolation for a better performance, and smaller pixel footprint.

We choose metal-insulator-metal (MIM) type plasmonic absorber to efficiently absorb LWIR radiation from object. At lower wavelength, it behaves like a near-perfect absorber. Where most other plasmonic absorbers see significant decrease towards LWIR after scaling, a MIM type absorber demonstrates highly efficient absorption by a sub-wavelength feature that is critical for our application to reduce the pixel dimensions. The transducing VO_2 nanobeam is buried within the insulator. The plasmonic absorption-induced thermal increase locally affects the VO_2 nanobeam. Even though, silicon dioxide can be used as the insulator layer, it exhibits lossy behavior over 7 μm wavelength. We choose magnesium fluoride as the insulator for optimal design at LWIR. Finally, in our design, the use of nanobeam instead of a thin-film [33]–[36] benefits the design in two ways. First, the large length to cross-section ratio amplifies the change in the readout voltage $\Delta V(T) = I_{bias}\rho_{NB}(T)L_{NB}/A_{NB}$ producing high responsivity, where L_{NB} and A_{NB} is the length and cross-sectional area of the VO_2 nanobeam, ρ_{NB} is the temperature dependent resistivity of high-TCR VO_2, I_{bias} is the bias current, and ΔV is the readout voltage. Second, since the bandwidth of thermal detectors are mainly determined by thermal mass and thermal conductance, the use of nanobeam instead of a film achieves a reduced pixel thermal mass thus an increase in the speed or bandwidth. Additionally, we propose to bias the device temperature at the phase transition point of VO_2 to utilize the high-TCR property of VO_2. At transition, the TCR can be as high as 200 K^{-1} [17], [18], [37] whereas other commonly used materials has a TCR below 3 K^{-1} [18]. However, due to hysteresis, the resistance-temperature fluctuation will result in micro-hysteresis [17], [18], [37], which is deterministic, and can be considered to calibrate the voltage readout. In following subsections, we will provide the details of individual components in design and performance point of view.

Sub-wavelength plasmonic features have spurred significant research interest and enabled novel applications such as radiation detection, spectroscopy, and sensing [11], [38]–[40]. Similarly, plasmonic absorbers [33], [34], [39], [41], [42] have the potential to enhance radiation absorption efficiency of thermal or infrared detectors that we are proposing while maintaining smaller pixel dimensions. Hence, these absorbers facilitate higher thermal buildup that is inversely proportional to the material volume and lead to a higher resistivity change of the transducing material. However, not all plasmonic absorbers are efficient over a wide range of wavelengths even after scaling the geometry. We choose metal-insulator-metal (MIM) type plasmonic structure that exhibits near perfect absorption [39] for short-wave infrared (SWIR), mid-wave infrared (MWIR) and over 55% absorptance at 10 μm wavelength or at long-wave infrared (LWIR). The schematic of the absorber in the unit cell is shown in Fig. 1(b). In the proposed MIM absorber, the metal layer is chosen to be gold and the insulator layer is chosen to be silicon dioxide (SiO_2) or magnesium fluoride (MgF_2). The top metal layer can be an array of circular or square patches in general. For optimized absorption at the 10 μm wavelength, we choose
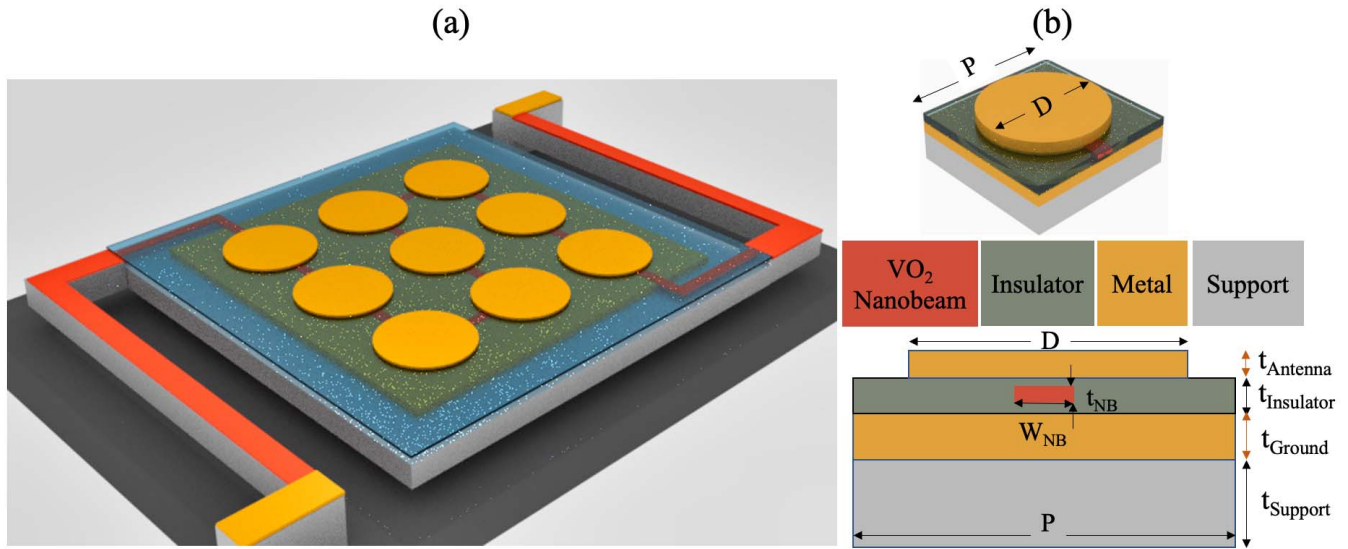
Fig. 1. (a) Schematic of a single bolometer pixel showing the support structure, suspension arms, plasmonic array of 3×3-unit cells as selective radiation absorber. The translucent blue layer is the insulator where the nanobeam is buried. (b) Plasmonic absorber unit cell with the VO_2 nanobeam buried within the insulator of a metal-insulator-metal (MIM) type absorber and the cross-sectional view of the unit cell with material layer thicknesses. In our default design, to obtain maximum absorptance at 10 μm wavelength, antenna and ground layers are chosen to be gold (Au) with $t_{Antenna}$ = 20 nm and t_{Ground} = 50 nm. Nanobeam transducing material is vanadium dioxide (VO_2) with t_{NB} = 20 nm and W_{NB} = 100 nm, insulator layer is magnesium fluoride (MgF_2) with $t_{Insulator}$ = 30 nm, and support layer is silicon nitride (Si_3N_4) with $t_{Support}$ = 200 nm. The default disk antenna diameter, D = 2.6 μm and unit cell period, P = 3 μm.
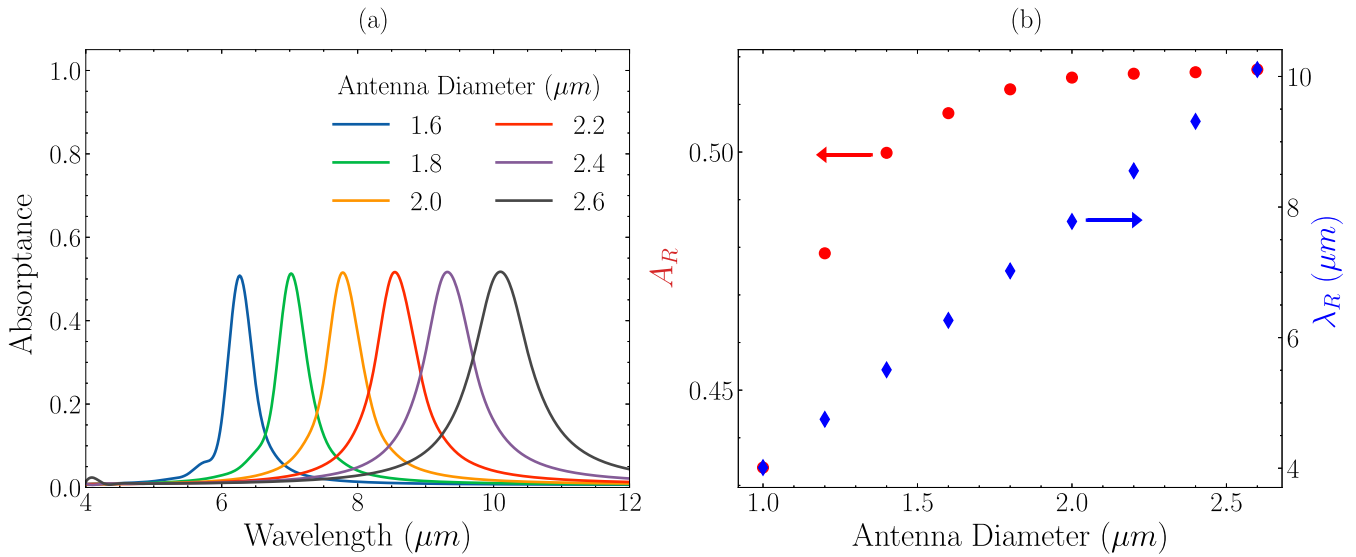

Fig. 2. Effect of duty cycle or diameter variation when the period is 3 μm - (a) the absorption spectrum for varying antenna diameter showing tunability of peak absorption wavelength i.e., the range of object temperature, (b) effect of antenna diameter variation on the peak absorptance, A_R (left axis – red) and the resonant wavelength, λ_R (right axis – blue).

circular patch with a diameter of 2.6 μm which are placed periodically at a 3 μm pitch. Since SiO_2 becomes highly reflective between 8-12 μm (Restrahlen band) and loses its ideal insulating behavior, it is not usable as an insulator layer for this wavelength range. However, fluorides of calcium or magnesium offer insulation over a wider wavelength range for LWIR applications. The key design parameters for the MIM absorber are – period (can be finite or infinite, latter for theoretical simplification of calculation and numerical analysis), top metal layer antenna diameter, insulator or spacer layer thickness and material (i.e., real and imaginary part of

optical index), metal thicknesses at ground plane and antenna layer. The presence of the VO_2 nanobeam, in both - semi-conducting and metallic states, has insignificant contribution to a change in the absorptance profile of MIM absorber. This is due to nanobeam's comparatively much smaller dimension than the wavelength and other features in the absorber. The reported absorption spectrums (obtained by optical simulation using COMSOL Multiphysics) in Fig. 2-4 present the effects of each of the design parameters by neglecting the insignificant variation caused by the presence of buried VO_2 nanobeam.
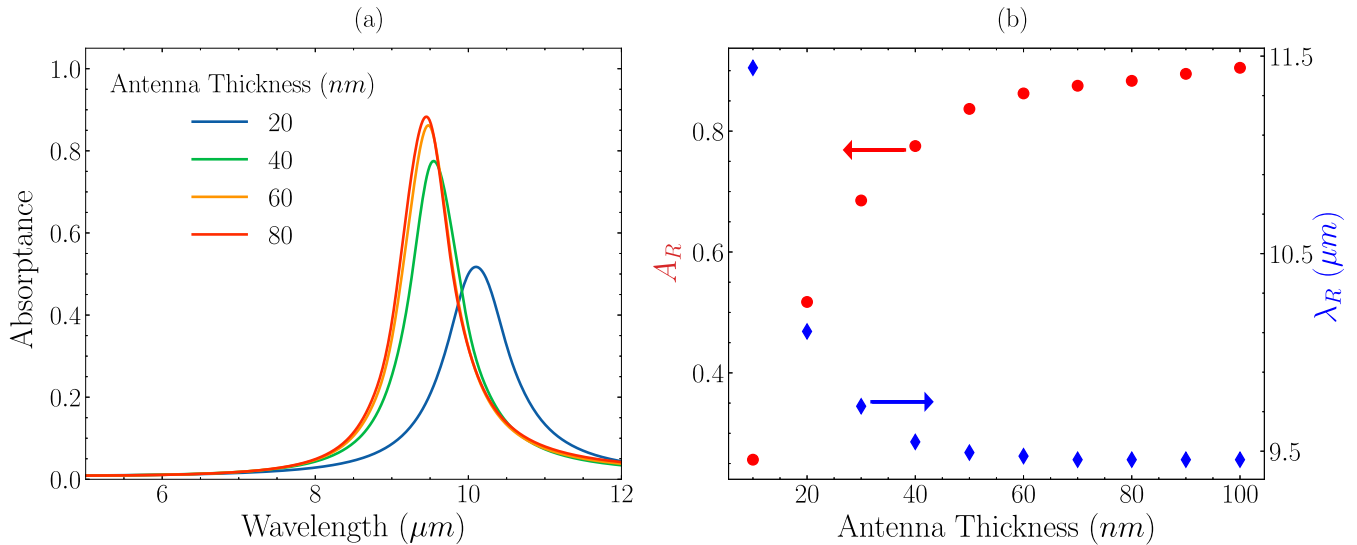
Fig. 3. Effect of antenna thickness with unit cell period fixed at 3 μm and antenna diameter fixed at 2.6 μm – (a) absorptance profile vs wavelength for thickness of the antenna or top metal layer, (b) absorptance, A_R (left axis – red) and wavelength, λ_R (right axis – blue) at resonance for a range of antenna thickness.
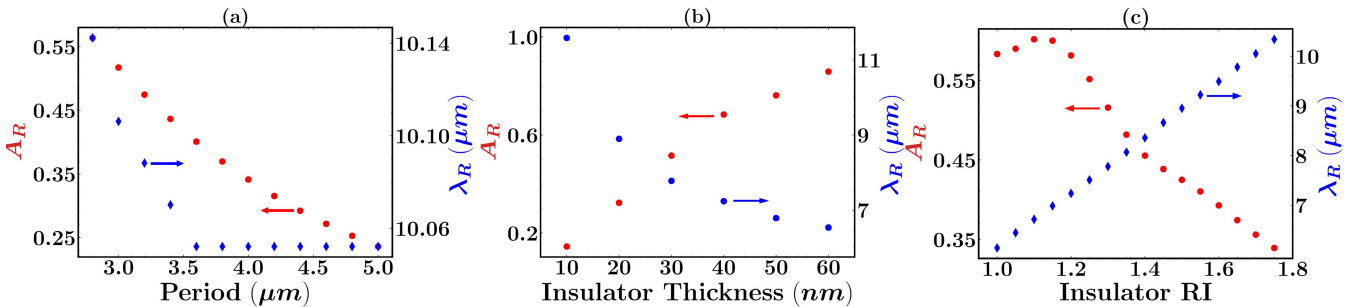

Fig. 4. Peak absorptance, A_R (left axis – red) and the wavelength of peak absorptance, λ_R (right axis – blue) with respect to (a) period of absorber unit cell, (b) insulator thickness, and (c) insulator refractive index (RI) keeping all the other design parameters at default value.

The resonance wavelength of the plasmonic antenna, or the peak absorption wavelength can be engineered by tailoring the antenna dimensions. Fig. 2 presents the absorption spectrum for different diameters of the circular gold (Au) antennas. However, depending on the fabrication process and required deposition temperature of VO$_2$, refractory metals like tungsten and platinum can also be used particularly for the ground metal plane. We have also investigated copper (Cu), silver (Ag), tungsten (W), and platinum (Pt) as the antenna and ground metal plane. We report the results for gold as it has the most favorable optical properties at the targeted 10 μm wavelength. Fig. 2(b) presents the variations in peak absorption efficiency, A_R and resonance wavelength, λ_R for different antenna diameters as can be related with Fig. 2(a). The red markers present the value of resonant absorptance (left y-axis), and the blue markers present the value of resonant wavelength (right y-axis). As expected, the resonance wavelength is blue shifted with the decreasing antenna diameter [36]. We anticipate higher absorption efficiency at lower wavelengths. The nearly flat absorption efficiency in Fig. 2(b) is mainly due to decreasing fill factor since we kept the period same at 3 μm for all these calculations.

A thicker top metal patch improves absorption because of stronger plasmonic interaction as shown in Fig. 3. However, it also adds to thermal mass which is unexpected. However, we see over 55% absorptance for only a 20 nm thick gold layer as the top metal. The effect of the bottom or ground metal layer thickness is insignificant as reported in [43]. A thin bottom layer is desired for lower thermal mass, higher bandwidth as well as less heat spreading by the metal layer. Better thermal isolation and further reduction of heat spreading can be obtained with a discontinuous ground metal. However, it adds to the complexity and steps in the fabrication process. So, we focus to investigate the architecture with a continuous ground film across all unit cells in a single pixel.

In Fig. 4, we present the peak absorptance and related wavelength with respect to variation in other design parameters - period of absorber unit cell, insulator material properties, and thickness. The changes in the period of the arrayed structure only impacts the absorptance efficiency, not the peak absorbing wavelength. From Fig. 4(a), we observe larger absorptance for higher fill factor, $F = Antenna Diameter/Period$. The peak absorptance shows weak exponential decrease with the increase of unit cell period.
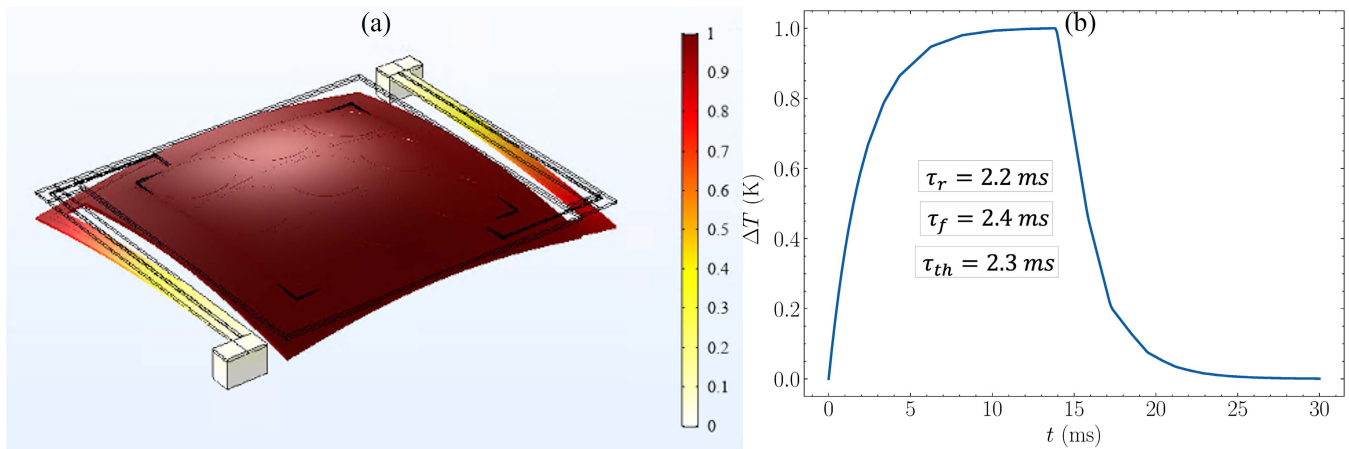
Fig. 5. (a) Thermal analysis of bolometer showing the temperature map of the bolometer for a 30 nW of heat flux incidence normal from the top, (b) Transient analysis of the thermal fluctuation of the detector in response to pulsed heat flux incidence. The thermal time constants for rising (τ_r) and falling (τ_f) edge are also calculated from this graph. The average thermal time constant, τ_{th} is calculated by averaging the rising and falling edge time constants.

The thickness and the material properties i.e., the refractive index of the insulator impact both – the resonant absorption wavelength as well as peak absorptance value. The effect of the insulator layer thickness is shown in Fig. 4(b). Thicker insulator is observed to allow higher absorptance. However, it adds to thermal mass of the pixel and can potentially degrade the overall performance of the detector. The relationship between peak absorptance wavelength and spacer refractive index is found to be linear (with slight variation due to numerical error) as also suggested by [34]. We also present the effect of the refractive index of the insulator layer material in Fig. 4(c) which shows that a lower range of refractive index allows higher peak absorptance and the resonant wavelength scales linearly with the insulator RI.

To enhance the responsivity, the device transducing material VO$_2$ nanobeam needs to operate at the transition point to have the highest TCR or sensitivity to temperature and radiation. We propose to operate the device at the transition point using a Peltier or thermo-electric heater to heat VO$_2$ nanobeam to the transition mid-point. Due to hysteresis of the phase transition in VO$_2$, the resistivity vs temperature will trace micro-hysteresis loops [18] for a small radiation fluctuation. However, the nature of the micro-hysteresis is expected to be deterministic as the material does not undergo any irreversible change.

A bolometer pixel is shown in Fig. 1(a). We choose a standard suspended pixel shape with two arms whose implementation can be further optimized which is beyond the scope of this work. We propose an arrangement of 3×3 array of absorber unit cells in a pixel with the VO$_2$ nanobeam spiral-traced below the absorbers and buried within the insulator layer. The nanobeam is 20 nm thick and 100 nm wide. This is an optimization between thermal and spatial resolution as mentioned earlier. The number of unit cell is chosen for sufficient radiation absorption to obtain high responsivity at the same time reducing the pixel pitch compared to state-of-the-art reports [44]–[49].

The radiation emitted from the object, after being focused by lenses on the pixels, gets absorbed by the plasmonic absorber elements in a pixel. Local heating and temperature buildup occur due to the radiation absorption. The local temperature buildup causes the local portion of the nanobeam to undergo changes in resistivity depending on the temperature level. This change in resistivity carries the information of the radiation emitted from the object. The change is read out from properly biased individual pixels to finally create a thermal map of the object in focus.

Thermal conductance, G_{th} and heat capacity, C_{th} are the two key parameters for a bolometer design and performance. Lower thermal conductance allows larger thermal buildup that results in higher sensitivity infrared detection. This can be achieved by eliminating the heat escape mechanisms. Thus, the ideal limit of performance is the radiative limit. The heat escape can be reduced by implementing structure that demote heat escape by conductance, for example, using suspended membrane to reduce vertical heat transfer and using long, thin and narrow arms to reduce lateral heat transfer, and so on. However, the thermal time constant of the detector is inversely proportional to the thermal conductance and directly proportional to the thermal resistance R_{th}: $\tau_{th} = C_{th}/G_{th} = C_{th} R_{th}$. Therefore, there is a tradeoff between the detection bandwidth and the heat capacity. The time constant directly defines the upper limit of the refresh rate in thermal cameras.

To obtain the thermal conductance of the proposed detector pixel, we calculate the amount of heat flux needed to raise the average temperature of the detector pixel by 1 K. We find the heat flux to be 30 nW per pixel area, resulting in a thermal conductance, $G_{th} = 3 \times 10^{-8}$ W/K. The thermal profile obtained using COMSOL Multiphysics is shown in Fig. 5(a). Such low value of thermal conductance combined with high TCR of the VO$_2$ nanobeam allows the detection of very low radiation power emitted from the object of interest. This high sensitivity makes it possible even to distinguish tiny temperature differences or a low NETD discussed on a later section. The displacement of the pixel in the figure is an exaggerated representation of the thermal response (in this case, only expansion) of the materials. We calculate the heat capacity to be 8.02×10^{-11} J/K and the corresponding thermal
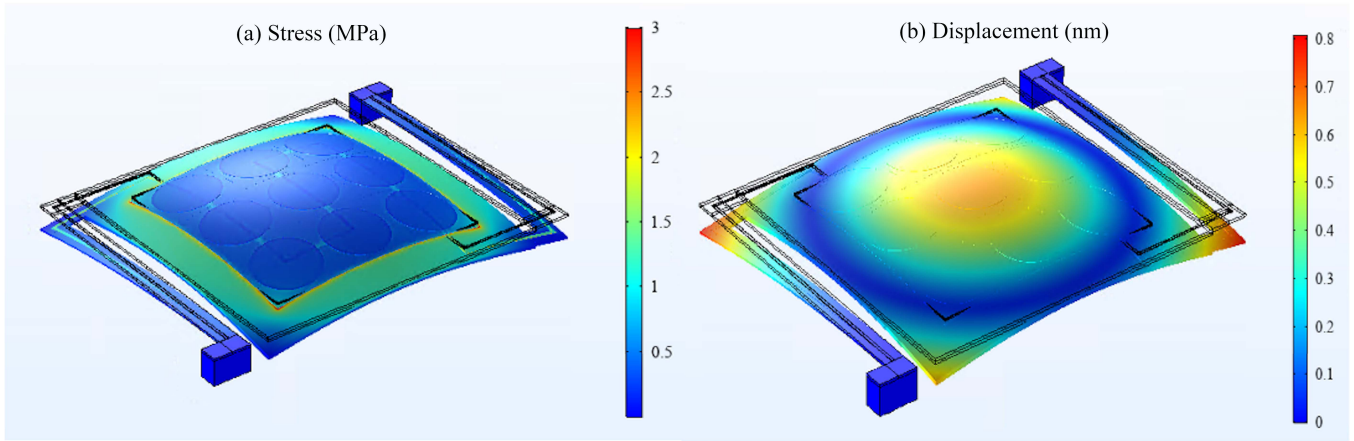
Fig. 6.   (a) Von Mises stress map of the detector showing critical regions of stress and (b) Displacement due to 30 nW of radiation incidence considering the thermal expansion coefficients of the materials in the bolometric detector.

time constant of 2.67 ms of the detector according to -

$$C_{th} = \sum_{layers} C_i \rho_i t_i A_d \qquad (1)$$

where, C indicates heat capacity, ρ is density, t is the thickness, A_d is the area of each material layer in a pixel. We conduct numerical transient analysis to extract the thermal time constant of the detector. A square pulsed radiation of 30 nW and 30 ms period is considered to be incident on the detector pixel and the corresponding temperature buildup is calculated numerically. The simulated time response is shown in Fig. 5(b). From the figure, we observe an average thermal time constant of 2.3 ms which is in close agreement with the previously calculated value. Due to smaller pixel dimension and reduced thermal mass in our design, the time constant is smaller than recent reports [44], [46], [47], [49]. The thermal time constant defines the minimum response time or maximum bandwidth of the detector. The thermal bandwidth of the detector is calculated to be 108 Hz from the thermal time constant using $BW = \frac{1}{4\tau_{th}}$ [50]. The electrical bandwidth is defined by the integration time, and the final output bandwidth depends on the frame rate.

The bolometer detector needs to be suspended to reduce conductive heat escape to the substrate and surrounding. We consider a 200 nm thick silicon nitride layer as the support as this material is commonly used for micro electro-mechanical system (MEMS) structures. The low thermal conductivity of silicon nitride allows the device to have low thermal conductance to ultimately obtain a high responsivity. Fig. 6 shows the numerical results for expected stress and displacement of the detector structure. The stress along the detector structure is below 3 MPa which is 2 to 3 orders lower than reported endurance limit of support nitride membrane [51], [52]. Hence, the structure will allow cyclic stress developed upon radiation fluctuations. Also, the displacement for thermal expansion of the materials is below 1 nm. Thus, the detector is mechanically stable and is expected to withstand periodic expansion and compression due to radiation exposure.

III. PERFORMANCE

To assess the performance of the bolometer we look at its responsivity and the noise equivalent power. The responsivity of bolometer is defined as the voltage signal generated for a 1 W of incident power. It is defined as R_v –

$$R_v = \frac{K \epsilon R_{th}}{\sqrt{(1 + \omega^2 \tau_{th}^2)}} \qquad (2)$$

Here, $K = I_{bias} \times R_{NB} \times TCR$, where I_{bias} is the bias current, which is considered to be 1 μA (to limit the Joule heating induced temperature change of the detector) through the analysis if not otherwise mentioned, R_{NB} is the nanobeam resistance, TCR is the temperature coefficient of resistance of the VO$_2$ nanobeam, ϵ is the emissivity of absorbing antennas, R_{th} is the thermal resistance, ω is the angular frequency, τ_{th} is the thermal time constant of the detector pixel. The responsivity of the detector is thus inversely proportional to the nanobeam cross-sectional area and proportional to the length. Hence, a detector with transducing nanobeams instead of a film thus facilitates higher responsivity. As an example, a nanobeam incorporated in our proposed 12 μm × 12 μm detector pixel will allow 270× responsivity compared to a film with the same thickness as the nanobeam (but different length to cross-sectional ratio) incorporated in the same pixel. The expected responsivity of the detector vs frequency is shown in Fig. 7(a). At a frequency of 100 Hz, we expect a responsivity of over 700 kV/W. As stated before, we are biasing the VO$_2$ nanobeam at the transition temperature. The responsivity is proportional to the TCR of the transducing material which in turn depend on the device bias temperature. The TCR of VO$_2$ can reduce by two orders of magnitude from on-transition to off-transition temperature [37]. As a result, the responsivity can degrade by up to two orders of magnitude if it is biased far from the transition temperature.

The radiative limit of responsivity, which is the theoretical performance limit of the device is shown in Fig. 7(b). Also, the noise equivalent power (NEP), defined as the signal level that produces a signal-to-noise ratio (SNR) of 1, is also presented. The NEP calculated for the proposed detector
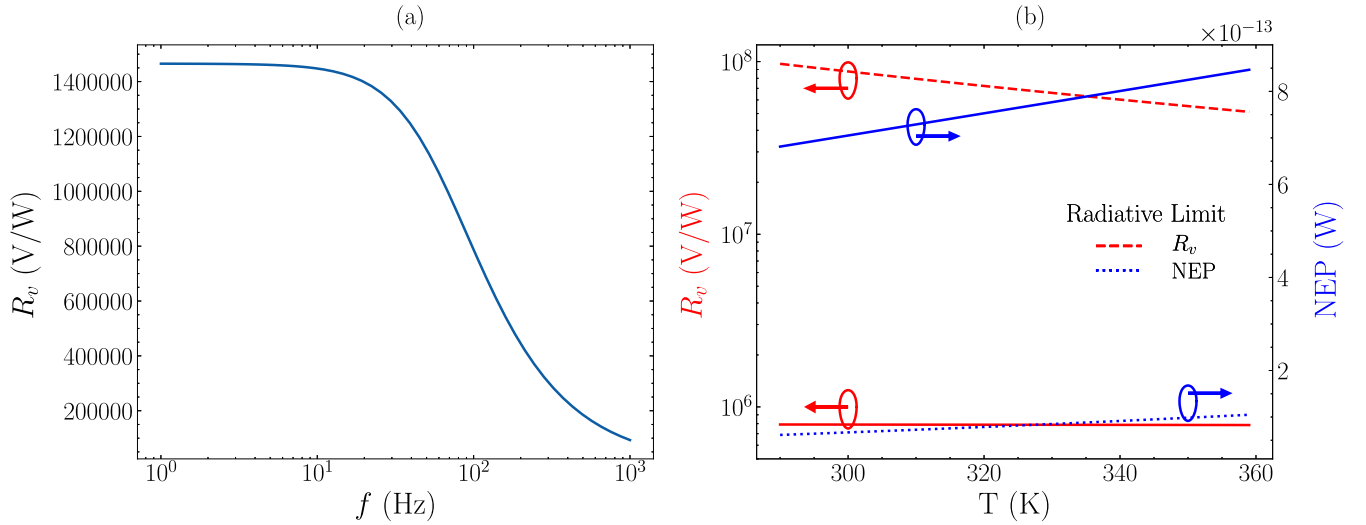
Fig. 7. (a) Responsivity with respect to frequency at 341 K temperature (device bias temperature to be at VO$_2$ transition). We estimate over 700 kV/W of responsivity at 100 Hz. (b) Responsivity (left y-axis, red) and NEP (right y-axis, blue) at 100 Hz along with their theoretical (radiative) limit with respect to device temperature.

design is very close to the radiative limit. The gap between the proposed detector and theoretical limit comes from the difference in radiative-only thermal conductance and detector thermal conductance.

The major sources of noise in a bolometer detector are Johnson or resistive noise (V_j), thermal fluctuation noise (V_{th}), flicker noise ($V_{1/f}$), and background noise (V_b). Johnson noise is a white noise and arises from the detector resistance and is proportional to the device bias temperature. It is defined as, $V_j = \sqrt{4kTR\Delta f}$, where k is Boltzmann constant, T is detector temperature, R is resistance mainly defined by the nanobeam resistance, and Δf is the bandwidth. The major component of the resistance is the VO$_2$ nanobeam itself. However, by biasing the device at the transition temperature of VO$_2$, the resistivity of the nanobeam VO$_2$ can be reduced by two orders of magnitude compared to its room-temperature semiconductor phase resistivity. This results in decrease of the Johnson noise and ultimately compensate for the noise development due to increased device temperature. Thus, the overall Johnson noise depends on the bandwidth, operating temperature, and the resistance of the device.

Thermal fluctuation noise arises from the temperature fluctuation of the detector. It is proportional to the thermal resistance. As a result, the effort to improve the sensitivity by increasing thermal resistance also increases the thermal fluctuation noise. The temperature fluctuation, ΔT of the device causes correspoding thermal fluctuation voltage, V_{th} to appear as noise contribution and is expressed as in equation (3). For our proposed design parameters, we observe this noise to be in the level of tens of micro-volts for a given device temperature of 341 K and at a frequency of 100 Hz.

$$V_{th} = \sqrt{K^2 \Delta \bar{T}^2} = 2KT\sqrt{\frac{k\Delta f}{(1+\omega^2\tau_{th}^2)}R_{th}} \qquad (3)$$

Another source of noise - the background noise, V_b is the noise due to radiative heat exchange between the detector

with temperature, T_d and surrounding background with a temperature T_b. It is expressed as -

$$V_b = \sqrt{\frac{8k\epsilon\sigma A(T_d^2 + T_b^2)}{(1+\omega^2\tau_{th}^2)}}KR_{th} \qquad (4)$$

where, σ is the Stefan-Boltzmann constant. Being in the order of 10^{-11} V over the frequency and bias temperature range of interest, this type of noise has insignificant contribution to the overall noise and thus can be neglected for the proposed detector.

All the noise components and their trend with respect to frequency and device temperature is presented in Fig. 8. Putting all the different noises together, thermal fluctuation noise is observed to be dominant. However, since the flicker noise is highly process and material dependent, we ignore its contribution [53]. Based on actual device fabrication parameters this type of noise should be added for completeness.

The detectivity and noise equivalent temperature difference (NETD) are also important performance metrics for an infrared thermal detector. The detectivity is defined as:

$$D^* = \frac{\sqrt{(A_d\Delta f)}}{NEP} = \frac{K\epsilon R_{th}\sqrt{A_d}}{\sqrt{(1+\omega^2\tau_{th}^2)(\frac{4kT^2K^2R_{th}}{1+\omega\tau_{th}^2} + 4kTR)}} \qquad (5)$$

where A_d is the active detector area. The obtained detectivity for the detector we propose is shown in Fig. 9. It is presented with respect to frequency, bias temperature, and thermal conductance. From Fig. 9(a), it is observed that device temperature has insignificant impact on the detectivity. This is due to large coefficient, K and large thermal resistance, R_{th} as they appear in equation 5. The detectivity with respect to the thermal conductance is presented in Fig. 9(b) as a reference to theoretical limit when G_{th} reaches its minimum possible value which is the case when only radiative thermal conductance is considered. Thermal conductance in our design of bolometer
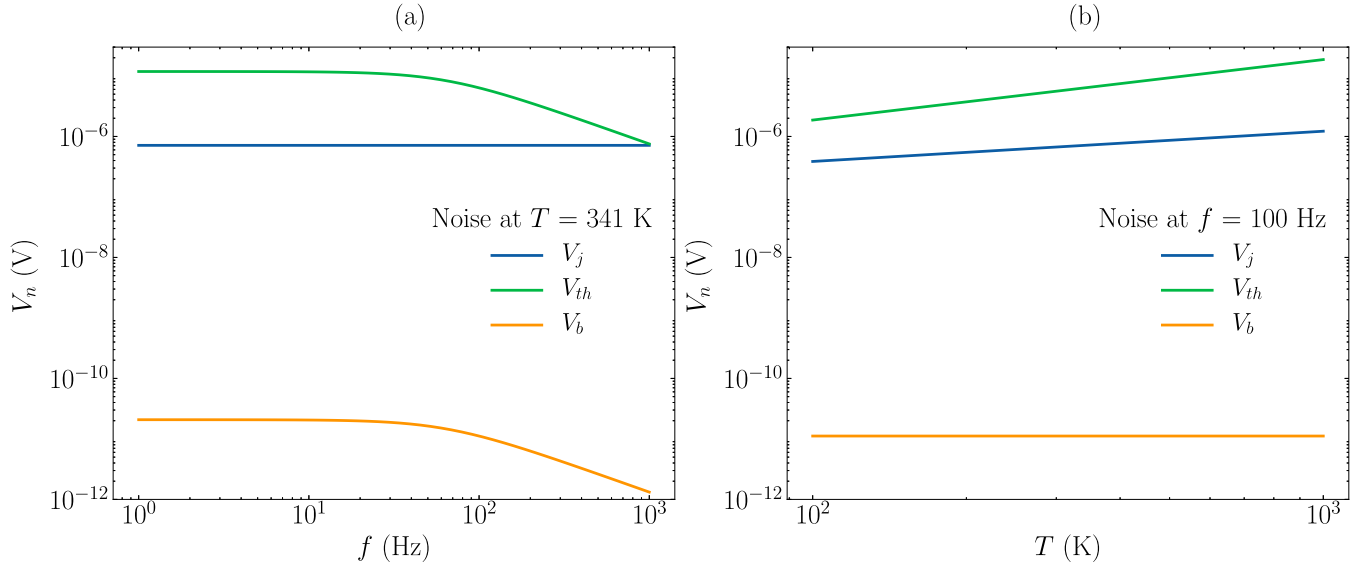
Fig. 8. All noise sources with respect to (a) frequency at bolometer temperature of 341 K and (b) bolometer temperature at a frequency of 100 Hz.
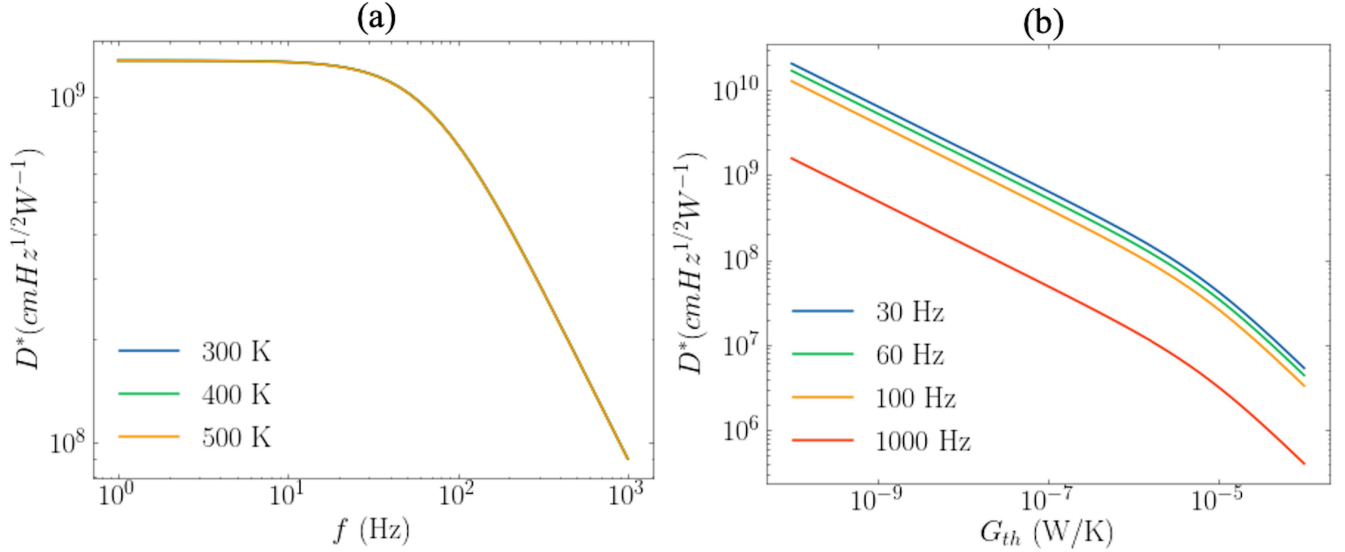

Fig. 9. Detectivity with respect to (a) frequency at $G_{th} = 30$ nW at different temperature level, and (b) thermal conductance of the bolometer at $T = 341$ K showing the performance limit in terms of detectivity.

pixel is 30 nW. As implied in Fig. 9(b), with improved design of the pixel arm, suspension, vacuum, and thermal isolation, detectivity can be improved further. Detectivity for 30 Hz and 60 Hz frequency is presented as they are two common refresh-rate currently used for visible wavelength and infrared cameras.

The NETD, on the other hand, is a measure of thermal resolution. It defines the minimum temperature difference that is distinguishable by the detector and is expresses as [53]

$$NETD = 4\left(\frac{F}{\#}\right)^2 \sqrt{\frac{\Delta f}{A_d}} \left[\int_{\lambda_a}^{\lambda_b} \frac{\partial M(\lambda)}{\partial T} D^*(\lambda)\, d\lambda\right]^{-1} \quad (6)$$

where, $\frac{F}{\#}$ is the aperture F-number, M is radiant exitance, λ is wavelength. For a bandwidth, Δf of 100 Hz and $\frac{F}{\#}$ of 1, integral wavelength limits of 8 to 10 μm, we obtain an NETD of 3.67 mK which is almost an order lower than the state-of-the-art detectors [44]–[46], [48], [49], [54] implemented in a smaller pixel.

We compare the proposed detector performance with some recent works and state-of-the-art bolometric uncooled detector. Our design is estimated to have a responsivity of over 700 kV/W at lower frequency which is a significant improvement over the recently reported detectors [44]–[46], [48], [49]. The recently demonstrated detector pixel size is 17 μm × 17 μm [45], [46], [49]. Our design requires the pixel size to be 12 μm × 12 μm while at the same time providing improved

TABLE I
COMPARISON TO OTHER RECENT WORKS

Figure of Merit	This Work	[44]	[45]	[46]	[47]	[48]	[49]
D^*(cmHz$^{1/2}$W^{-1})	1.2×10^9	5.4×10^8	NR	NR	1.0×10^7	NR	2.2×10^8
R_v(V/W)	>7×10^5	5×10^4	NR	NR	1×10^4	NR	5×10^5
τ_{th}(ms)	2.3	5.3	NR	5.9	<10	NR	4.5
Area (μm × μm)	12×12	40×40	17×17	17×17	35×35	35×35	17×17
G_{th}(nW/K)	30	NR	NR	40	700	NR	62
NETD (mK)	3.67	NR	35	NR	NR	71	NR
NEP (pW)	1	NR	NR	NR	NR	NR	100

performance in terms of detectivity, responsivity, NETD. The NEP is estimated to be very close to the theoretical limit. In Table I, we show the summary of the comparison (NR stands for not reported). It is observed that, our proposed design shows improvement in every possible angle even where it is very challenging due to the design dilemma between different parameters.

We acknowledge that the properties of VO$_2$ is dependent on fabrication process especially temperature, substrate, strain, and geometry [55]–[60]. In addition, VO$_2$ nanostructure (nanowire and nanobeam) resistivity along with its relationship with respect to temperature depends on its geometry and can differ from bulk and thin-film properties by up to an order of magnitude [55]–[57], [59]. The resistivity impacts device responsivity and noise performance. The final design, particularly the nanobeam geometry needs to be optimized by taking into consideration the variations in fabrication process. Most studies [55], [59]–[62] on VO$_2$ nanostructures focus on the mechanically transferred VO$_2$ nanowires and nanobeams after being synthesized using vapor transport method. However, random growth and subsequent transfer of VO$_2$ nanostructure is not suitable for our proposed design of bolometer pixel as the nanobeam traces integrated with the plasmonic absorbers need to be physically and electrically continuous and aligned with absorbers and electrical contacts. On the other hand, the use of lift-off technique for patterning the nanobeam traces is not suitable due to high deposition temperature of VO$_2$ films. Therfore, dry etching [63] of the sputtered VO$_2$ film to pattern the nanobeam is suggested.

IV. CONCLUSION

In this work, we propose a novel LWIR detector architecture with plasmonic absorber and VO$_2$ nanobeam integrated. The plasmonic absorber allows efficient and selective radiation detection from the radiating object. The design of the absorber can be scaled to tune the wavelength or temperature band of interest. Additionally, the sub-wavelength plasmonic features allow the detection of wavelength by a detector with a much smaller form-factor. The use of VO$_2$ nanobeam, instead of a simple VO$_2$ film, amplifies the slope of the temperature dependent resistance due to the large ratio between length to cross-sectional area of the nanobeam allowing high responsivity. The proposed design and estimated performance are desired for mission critical applications where high-sensitivity, high-bandwidth, and noise-immunity come as strict requirements such as thermal and medical imaging, night vision, detection and tracking, etc. We present the numerical analysis, noise analysis, and figure of merits of the proposed detector design. The structural, thermal and transient analysis of the bolometer are discussed. Whereas conventional approach trades off performance with active detector area; we observe significantly improved detectivity, NETD, responsivity for a detector of smaller form-factor. The design allows improvement in spatial resolution as well as thermal responsivity. We obtain a responsivity of over 700 kV/W at 100 Hz for only a 12 μm × 12 μm pixel size. The noise equivalent temperature difference for the proposed design is calculated to be as low as 3.67 mK, almost an order lower than detectors reported with larger pixel dimension.

REFERENCES

[1] A. Rogalski, J. Antoszewski, and L. Faraone, "Third-generation infrared photodetector arrays," *J. Appl. Phys.*, vol. 105, no. 9, May 2009, Art. no. 091101.

[2] S. Bianconi and H. Mohseni, "Recent advances in infrared imagers: Toward thermodynamic and quantum limits of photon sensitivity," *Rep. Prog. Phys.*, vol. 83, no. 4, Apr. 2020, Art. no. 044101.

[3] A. Rogalski, "Recent progress in infrared detector technologies," *Infr. Phys. Technol.*, vol. 54, no. 3, pp. 136–154, May 2011.

[4] D. Palaferri *et al.*, "Room-temperature nine-μm-wavelength photodetectors and GHz-frequency heterodyne receivers," *Nature*, vol. 556, no. 7699, pp. 85–88, Apr. 2018.

[5] C. L. Tan and H. Mohseni, "Emerging technologies for high performance infrared detectors," *Nanophotonics*, vol. 7, no. 1, pp. 169–197, Jan. 2018.

[6] R. McClintock, J. L. Pau, K. Minder, C. Bayram, P. Kung, and M. Razeghi, "Hole-initiated multiplication in back-illuminated GaN avalanche photodiodes," *Appl. Phys. Lett.*, vol. 90, no. 14, Apr. 2007, Art. no. 141112.

[7] O. Boyraz and B. Jalali, "Demonstration of a silicon Raman laser," *Opt. Exp.*, vol. 12, no. 21, pp. 5269–5273, 2004.

[8] V. Donzella, A. Sherwali, J. Flueckiger, S. T. Fard, S. M. Grist, and L. Chrostowski, "Sub-wavelength grating components for integrated optics applications on SOI chips," *Opt. Exp.*, vol. 22, no. 17, pp. 21037–21050, 2014.

[9] K. Xu, "Integrated silicon directly modulated light source using p-well in standard CMOS technology," *IEEE Sensors J.*, vol. 16, no. 16, pp. 6184–6191, Aug. 2016.

[10] K. Xu, "Silicon electro-optic micro-modulator fabricated in standard CMOS technology as components for all silicon monolithic integrated optoelectronic systems," *J. Micromech. Microeng.*, vol. 31, no. 5, May 2021, Art. no. 054001.

[11] Q. Zhao, M. W. Khan, S. Farzinazar, J. Lee, and O. Boyraz, "Plasmo-thermomechanical radiation detector with on-chip optical readout," *Opt. Exp.*, vol. 26, no. 23, pp. 29638–29650, 2018.

[12] M. W. Khan, P. Sadri-Moshkenani, M. S. Islam, and O. Boyraz, "Graphene-coated suspended metallic nanostructures for fast and sensitive optomechanical infrared detection," in *CLEO: Science and Innovations*, Washington, DC, USA: Optical Society of America, May 2019, pp. JTu2A–51.

[13] M. W. Khan, Q. Zhao, P. Sadri-Moshkenani, M. S. Islam, and O. Boyraz, "Graphene-incorporated plasmo-thermomechanical infrared radiation detection," *J. Opt. Soc. Amer. B, Opt. Phys.*, vol. 37, no. 3, pp. 774–783, 2020.

[14] H. Choi, J. Ahn, J. Jung, T. Noh, and D. Kim, "Mid-infrared properties of a VO_2 film near the metal-insulator transition," *Phys. Rev. B, Condens. Matter*, vol. 54, no. 7, p. 4621, 1996.

[15] N. Émond, A. Hendaoui, and M. Chaker, "Low resistivity $W_X V_{1-X} O_2$-based multilayer structure with high temperature coefficient of resistance for microbolometer applications," *Appl. Phys. Lett.*, vol. 107, no. 14, Oct. 2015, Art. no. 143507.

[16] B. Wang, J. Lai, H. Li, H. Hu, and S. Chen, "Nanostructured vanadium oxide thin film with high TCR at room temperature for microbolometer," *Infr. Phys. Technol.*, vol. 57, pp. 8–13, Mar. 2013.

[17] C. D. Reintsema, E. N. Grossman, and J. A. Koch, "Improved VO_2 microbolometers for infrared imaging: Operation on the semiconducting-metallic phase transition with negative electrothermal feedback," *Proc. SPIE*, vol. 3698, pp. 190–200, Jul. 1999

[18] L. A. L. de Almeida, G. S. Deep, A. M. Nogueira-Lima, and H. Neff, "Modeling of the hysteretic metal-insulator transition in a vanadium dioxide infrared detector," *Opt. Eng.*, vol. 41, no. 10, pp. 2582–2588, 2002.

[19] S. Chen, H. Ma, S. Xiang, and X. Yi, "Fabrication and performance of microbolometer arrays based on nanostructured vanadium oxide thin films," *Smart Mater. Struct.*, vol. 16, no. 3, p. 696, 2007.

[20] J. Gou, J. Wang, X. Zheng, D. Gu, H. Yu, and Y. Jiang, "Detection of terahertz radiation from 2.52 THz CO_2 laser using a 320×240 vanadium oxide microbolometer focal plane array," *RSC Adv.*, vol. 5, no. 102, pp. 84252–84256, 2015.

[21] T. D. Dao *et al.*, "MEMS-based wavelength-selective bolometers," *Micromachines*, vol. 10, no. 6, p. 416, Jun. 2019.

[22] E. Smith, "Vanadium oxide microbolometers with patterned gold black or plasmonic resonant absorbers," Ph.D. dissertation, Dept. Phys., College Sci., Univ. Central Florida, Orlando, FL, USA, 2015.

[23] E. E. Chain, "Optical properties of vanadium dioxide and vanadium pentoxide thin films," *Appl. Opt.*, vol. 30, no. 19, pp. 2782–2787, 1991.

[24] C. H. Griffiths and H. K. Eastwood, "Influence of stoichiometry on the metal-semiconductor transition in vanadium dioxide," *J. Appl. Phys.*, vol. 45, no. 5, pp. 2201–2206, May 1974.

[25] E. Kusano, J. Theil, and J. A. Thornton, "Deposition of vanadium oxide films by direct-current magnetron reactive sputtering," *J. Vac. Sci. Technol. A, Vac., Surf., Films*, vol. 6, no. 3, pp. 1663–1667, 1988.

[26] P. Jin and S. Tanemura, "Formation and thermochromism of VO_2 films deposited by RF magnetron sputtering at low substrate temperature," *Jpn. J. Appl. Phys.*, vol. 33, no. 3R, p. 1478, 1994.

[27] R. Shi *et al.*, "Recent advances in fabrication strategies, phase transition modulation, and advanced applications of vanadium dioxide," *Appl. Phys. Rev.*, vol. 6, no. 1, Mar. 2019, Art. no. 011312.

[28] R. Shi *et al.*, "Axial modulation of metal–insulator phase transition of VO_2 nanowires by graded doping engineering for optically readable thermometers," *J. Phys. Chem. C*, vol. 121, no. 44, pp. 24877–24885, 2017.

[29] S. Korkmaz, M. Turkmen, and S. Aksu, "Mid-infrared narrow band plasmonic perfect absorber for vibrational spectroscopy," *Sens. Actuators A, Phys.*, vol. 301, Jan. 2020, Art. no. 111757.

[30] S. Wang, Y. Wang, S. Zhang, and W. Zheng, "Mid-infrared broadband absorber of full semiconductor epi-layers," *Phys. Lett. A*, vol. 381, no. 16, pp. 1439–1444, Apr. 2017.

[31] L. Nordin, A. Kamboj, P. Petluru, E. Shaner, and D. Wasserman, "All-epitaxial integration of long-wavelength infrared plasmonic materials and detectors for enhanced responsivity," *ACS Photon.*, vol. 7, no. 8, pp. 1950–1956, Aug. 2020.

[32] S. Ogawa, J. Komoda, K. Masuda, and M. Kimata, "Wavelength selective wideband uncooled infrared sensor using a two-dimensional plasmonic absorber," *Opt. Eng.*, vol. 52, no. 12, Dec. 2013, Art. no. 127104.

[33] S. Calhoun *et al.*, "Multispectral plasmonic perfect absorbers integrated with room-temperature VO_X air-bridge bolometers," in *Proc. IEEE Res. Appl. Photon. Defense Conf. (RAPID)*, Aug. 2019, pp. 1–2.

[34] R. N. Evans, S. R. Calhoun, J. W. Cleary, E. M. Smith, and R. E. Peale, "Far-infrared bands in plasmonic metal-insulator-metal absorbers optimized for long-wave infrared," *MRS Adv.*, vol. 4, nos. 11–12, pp. 667–674, Feb. 2019.

[35] E. M. Smith *et al.*, "Linear bolometer array using a high TCR VO_X-Au film," *Proc. SPIE*, vol. 9070. Jun. 2014, Art. no. 90701Z.

[36] J. W. Cleary, R. E. Peale, E. Smith, and J. Nath, "Wavelength-selective thermal detection apparatus and methods," U.S. Patent 10 101 212, Oct. 16, 2018.

[37] L. A. L. de Almeida, G. S. Deep, A. M. N. Lima, I. A. Khrebtov, V. G. Malyarov, and H. Neff, "Modeling and performance of vanadium–oxide transition edge microbolometers," *Appl. Phys. Lett.*, vol. 85, no. 16, pp. 3605–3607, Oct. 2004.

[38] A. Ahmed, H. Kim, J. Kim, K. Hwang, and S. Kim, "Enhancing the responsivity of uncooled infrared detectors using plasmonics for high-performance infrared spectroscopy," *Sensors*, vol. 17, no. 4, p. 908, Apr. 2017.

[39] N. Liu, M. Mesch, T. Weiss, M. Hentschel, and H. Giessen, "Infrared perfect absorber and its application as plasmonic sensor," *Nano Lett.*, vol. 10, no. 7, pp. 2342–2348, Jul. 2010.

[40] V. Belotelov *et al.*, "Enhanced magneto-optical effects in magnetoplasmonic crystals," *Nature Nanotechnol.*, vol. 6, no. 6, p. 370, 2011.

[41] C.-W. Cheng, M. N. Abbas, C.-W. Chiu, K.-T. Lai, M.-H. Shih, and Y.-C. Chang, "Wide-angle polarization independent infrared broadband absorbers based on metallic multi-sized disk arrays," *Opt. Exp.*, vol. 20, no. 9, pp. 10376–10381, 2012.

[42] A. Haque *et al.*, "Broadband and thermally stable tungsten boride absorber," *J. Opt. Soc. Amer. B, Opt. Phys.*, vol. 36, no. 10, pp. 2744–2749, 2019.

[43] M. W. Khan *et al.*, "Selective and efficient infrared detection by plasmonically heated vanadium-dioxide nanowire," *Proc. SPIE*, vol. 11462, Sep. 2020, Art. no. 114622S.

[44] O. Alkorjia *et al.*, "Metasurface based uncooled microbolometer with high fill factor," in *Proc. 20th Int. Conf. Solid-State Sensors, Actuat. Microsyst. Eurosensors XXXIII (TRANSDUCERS EUROSENSORS XXXIII)*, Jun. 2019, pp. 2126–2129.

[45] O. Celik *et al.*, "640×480 17 μm microbolometer uncooled detector development at ASELSAN, Inc," *Proc. SPIE*, vol. 11407, Apr. 2020, Art. no. 1140719.

[46] C. B. Kaynak *et al.*, "Thermo-mechanical modeling and experimental validation of an uncooled microbolometer," in *Proc. IEEE 20th Topical Meeting Silicon Monolithic Integr. Circuits RF Syst. (SiRF)*, Jan. 2020, pp. 57–59.

[47] E. M. Smith *et al.*, "Dual band sensitivity enhancements of a VO_X microbolometer array using a patterned gold black absorber," *Appl. Opt.*, vol. 55, no. 8, pp. 2071–2078, 2016.

[48] F. Tankut, M. H. Cologlu, H. Ozturk, G. Cilbir, O. S. Akar, and T. Akin, "A 160×120 LWIR-band CMOS infrared (CIR) microbolometer," *Proc. SPIE*, vol. 11002, May 2019, Art. no. 110021Q.

[49] T.-H. Yeh, C.-K. Tsai, S.-Y. Chu, H.-Y. Lee, and C.-T. Lee, "Performance improvement of Y-doped VO_X microbolometers with nanomesh antireflection layer," *Opt. Exp.*, vol. 28, no. 5, pp. 6433–6442, 2020.

[50] M. Kohin and N. R. Butler, "Performance limits of uncooled VO_X microbolometer focal plane arrays," *Proc. SPIE*, vol. 5406, pp. 447–453, Aug. 2004.

[51] T. Kawakubo and K. Komeya, "Static and cyclic fatigue behavior of a sintered silicon nitride at room temperature," *J. Amer. Ceram. Soc.*, vol. 70, no. 6, pp. 400–405, Jun. 1987.

[52] W.-H. Chuang, R. K. Fettig, and R. Ghodssi, "Nano-scale fatigue study of LPCVD silicon nitride thin films using a mechanical-amplifier actuator," *J. Micromech. Microeng.*, vol. 17, no. 5, p. 938, 2007.

[53] A. Rogalski, *Infrared Detectors*. Boca Raton, FL, USA: CRC Press, Nov. 2010.

[54] D. Benirschke and S. Howard, "Characterization of a low-cost, commercially available, vanadium oxide microbolometer array for spectroscopic imaging," *Opt. Eng.*, vol. 56, no. 4, Apr. 2017, Art. no. p. 040502.

[55] L. Hongwei *et al.*, "Size effects on metal-insulator phase transition in individual vanadium dioxide nanowires," *Opt. Exp.*, vol. 22, no. 25, pp. 30748–30755, 2014.

[56] V. Théry *et al.*, "Role of thermal strain in the metal-insulator and structural phase transition of epitaxial VO_2 films," *Phys. Rev. B, Condens. Matter*, vol. 93, no. 18, May 2016, Art. no. 184106.

[57] J. Wei, Z. Wang, W. Chen, and D. H. Cobden, "New aspects of the metal–insulator transition in single-domain vanadium dioxide nanobeams," *Nature Nanotechnol.*, vol. 4, no. 7, pp. 420–424, Jul. 2009.

[58] H. Wen *et al.*, "Structural and electronic recovery pathways of a photoexcited ultrathin VO_2 film," *Phys. Rev. B, Condens. Matter*, vol. 88, no. 16, Oct. 2013, Art. no. 165424.

[59] J. Wu, Q. Gu, B. S. Guiton, N. P. De Leon, L. Ouyang, and H. Park, "Strain-induced self organization of metal–insulator domains in single-crystalline VO_2 nanobeams," *Nano Lett.*, vol. 6, no. 10, pp. 2313–2317, 2006.

[60] C. Cheng, K. Liu, B. Xiang, J. Suh, and J. Wu, "Ultra-long, free-standing, single-crystalline vanadium dioxide micro/nanowires grown by simple thermal evaporation," *Appl. Phys. Lett.*, vol. 100, no. 10, Mar. 2012, Art. no. 103111.
[61] B. S. Guiton, Q. Gu, A. L. Prieto, M. S. Gudiksen, and H. Park, "Single-crystalline vanadium dioxide nanowires with rectangular cross sections," *J. Amer. Chem. Soc.*, vol. 127, no. 2, pp. 498–499, Jan. 2005.
[62] S. Rathi, J.-H. Park, I.-Y. Lee, J. M. Baik, K. S. Yi, and G.-H. Kim, "Unravelling the switching mechanisms in electric field induced insulator–metal transitions in VO$_2$ nanobeams," *J. Phys. D, Appl. Phys.*, vol. 47, no. 29, Jun. 2014, Art. no. 295101.
[63] A. Efremov, "Etching characteristics and mechanism of vanadium dioxide in inductively coupled Cl$_2$/Ar plasma," *J. Micro/Nanolithogr., MEMS, MOEMS*, vol. 8, no. 2, Apr. 2009, Art. no. 021110.

Jonathan Matthew Sullivan received the B.S. degree in mechanical and aerospace engineering from the University of California Irvine, Irvine, CA, USA, in 2017, where he is currently pursuing the Ph.D. degree with the Department of Mechanical and Aerospace Engineering. He has been working with the Nano Thermal Energy Research Group, UCI, since Spring 2016. His research interests include micro/nanoscale heat transport, radiative heat transfer, thermal management, and machine learning.

Jaeho Lee received the B.S. degree (Hons.) in mechanical engineering from the Georgia Institute of Technology in 2007, and the M.S. and Ph.D. degrees in mechanical engineering (electrical engineering) from Stanford University in 2012. He is currently an Assistant Professor with the Department of Mechanical and Aerospace Engineering, University of California Irvine, Irvine, CA, USA. He is also the Director of the Heat Transfer Innovations, Education, and Research Group, UCI. Prior to joining UC Irvine in 2015, he worked as a Post-Doctoral Scholar with Materials Sciences Division, Lawrence Berkeley National Laboratory. His research interests include thermal management, electronics cooling, energy harvesting, phase-change materials, and temperature sensing.

Mohammad Wahiduzzaman Khan received the B.S. degree in electrical and electronic engineering from the Bangladesh University of Engineering and Technology, Dhaka, Bangladesh, in 2014, and the M.S. degree in electrical and computer engineering from the University of California Irvine, Irvine, CA, USA, in 2021, where he is currently pursuing the Ph.D. degree with the Department of Electrical Engineering and Computer Science. He has been working with the Advanced Photonic Devices and Systems Laboratory, UC Irvine, since 2016. His research interests include optical sensing, infrared detectors, integrated optics, and silicon photonics.

Ozdal Boyraz received the M.S. and Ph.D. degrees from the University of Michigan, Ann Arbor, in 1997 and 2001, respectively. After two years of industrial experience with Xtera Communications, Allen, TX, USA, he joined the University of California, Los Angeles, USA, as a Post-Doctoral Research Fellow in 2003. In 2005, he joined the Electrical Engineering Department, University of California Irvine, Irvine, USA, as a Tenure Track Faculty. He has over 200 journal and conference publications and 6 issued patents. His research interests include silicon-based optoelectronic devices, nano photonics, optical communications systems, RF over fiber, nonlinear optics, and optical signal processing. He is a Senior Member of OSA. He was a recipient of the 2010 DARPA Young Faculty Award.